FULL PAPER

Magnetic Resonance in Medicine 00:00–00 (2017)

An Open 8-Channel Parallel Transmission Coil for Static and Dynamic 7T MRI of the Knee and Ankle Joints at Multiple Postures

Jin Jin,[1]* Ewald Weber,[1] Aurelien Destruel,[1] Kieran O'Brien,[2] Bassem Henin,[1] Craig Engstrom,[3] and Stuart Crozier[1]

Purpose: We present the initial in vivo imaging results of an open architecture eight-channel parallel transmission (pTx) transceive radiofrequency (RF) coil array that was designed and constructed for static and dynamic 7T MRI of the knee and ankle joints.

Methods: The pTx coil has a U-shaped dual-row configuration (200 mm overall length longitudinally) that allows static and dynamic imaging of the knee and ankle joints at various postures and during active movements. This coil structure, in combination with B_1 shimming, allows flexible configuration of B_1 transmit profiles, with good homogeneity over 120-mm regions of interest. This coil enabled high-resolution gradient echo (e.g., 3D dual-echo steady state [DESS] and 3D multiecho data image combination [MEDIC]) and turbo spin echo (TSE) imaging (e.g., with proton density weighting [PDw], PDw with fat saturation, and T_1 and T_2 weightings) with local RF energy absorption rates well below regulatory limits.

Results: High-resolution 2D and 3D image series (e.g., 0.3 mm in-plane resolution for TSE, 0.47 mm isotropic for DESS and MEDIC) were obtained from the knee and ankle joints with excellent tissue contrast. Dynamic imaging during continuous knee and ankle flexion-extension cycles were successfully acquired.

Conclusion: The new open pTx coil array provides versatility for high-quality static and dynamic MRI of the knee and ankle joints at 7T. **Magn Reson Med 000:000–000, 2017. © 2017 International Society for Magnetic Resonance in Medicine.**

Key words: ultra-high field MRI; musculoskeletal (MSK) imaging; parallel transmit (pTx) array; dynamic imaging; 7T in-vivo

INTRODUCTION

In MRI, higher field strengths provide higher signal-to-noise ratios to enable enhanced spatial resolution and/or reduced scan time for an overall improved imaging performance compared with lower fields (1). Optimal performance in ultrahigh field (UHF) MRI is highly dependent on radiofrequency (RF) coils tailored for specific anatomical regions and imaging applications. Currently, there is a limited number of RF coils for UHF human MRI (2), because UHF coil design needs to address inhomogeneous magnetic excitation and elevated local RF energy deposition. In UHF whole body applications, inhomogeneous excitation profiles often severely degrade image quality, (3) whereas global and local RF energy deposition as typically measured with specific absorption rate (SAR) can become substantially elevated (4–6).

The development of RF coil arrays at UHF with parallel transmission (pTx) capability provides a promising approach to balance the three competing factors of inhomogeneous excitation profiles, local SAR restrictions and limited peak RF power (typically 8 or 16 kW at the RF power amplifier level) (7). Specifically, pTx techniques (8,9) require independent control of the simultaneous transmission channels to tailor the RF waveforms and achieve a targeted excitation efficiently. B_1 shimming (10) optimizes the magnitudes and phases of the otherwise identical RF waveform from all channels and provides solutions to the aforementioned issues (7,11,12). When combined with these techniques, dedicated multichannel array coils with independent parallel channels offer an attractive solution for maximizing the performance of UHF MRI in humans.

Dedicated UHF RF coils for MRI of the musculoskeletal system have the capacity for superior signal-to-noise ratio, enabling higher spatial resolution to facilitate improved assessment of small structures with oblique orientation (13,14). In addition to providing conventional static images with excellent contrast between muscles, menisci, ligaments, and tendons (15,16), RF coils with innovative design offer avenues for dynamic (kinematic) imaging to investigate joints positioned in multiple postures and/or during active movement. Dynamic musculoskeletal imaging has been performed at lower fields (17), providing kinematic information not intrinsically available in static scans (18). Specifically, it allows examination of in vivo kinematics and interactions between tissues to assess aspects such as impingement, maltracking, or deformation of structures within and around complex joints such as the knee and ankle.

At present, commercial RF coils for musculoskeletal imaging at 7T are mostly limited to the knee and typically without pTx capability. Existing examples include the 1-Tx/28-Rx knee coil from Quality Electrodynamics (QED; Mayfield Village, Ohio, USA) (19,20), the transceive quadrature knee coils from In-Vivo Corporation (Gainesville, Florida, USA) (6,21) and Nova Medical

[1]School of Information Technology and Electrical Engineering, University of Queensland, Brisbane, Queensland, Australia.

[2]Siemens Healthcare, Brisbane, Australia.

[3]School of Human Movement and Nutrition Sciences, University of Queensland, Brisbane, Queensland, Australia.

*Correspondence to: Jin Jin, Ph.D., 523 GP South Building 78, Staff House Road, St Lucia, Queensland 4072, Australia. E-mail: jinjin@itee.uq.edu.au

Received 9 May 2017; revised 28 May 2017; accepted 30 May 2017

DOI 10.1002/mrm.26804

Published online 00 Month 2017 in Wiley Online Library (wileyonlinelibrary.com).

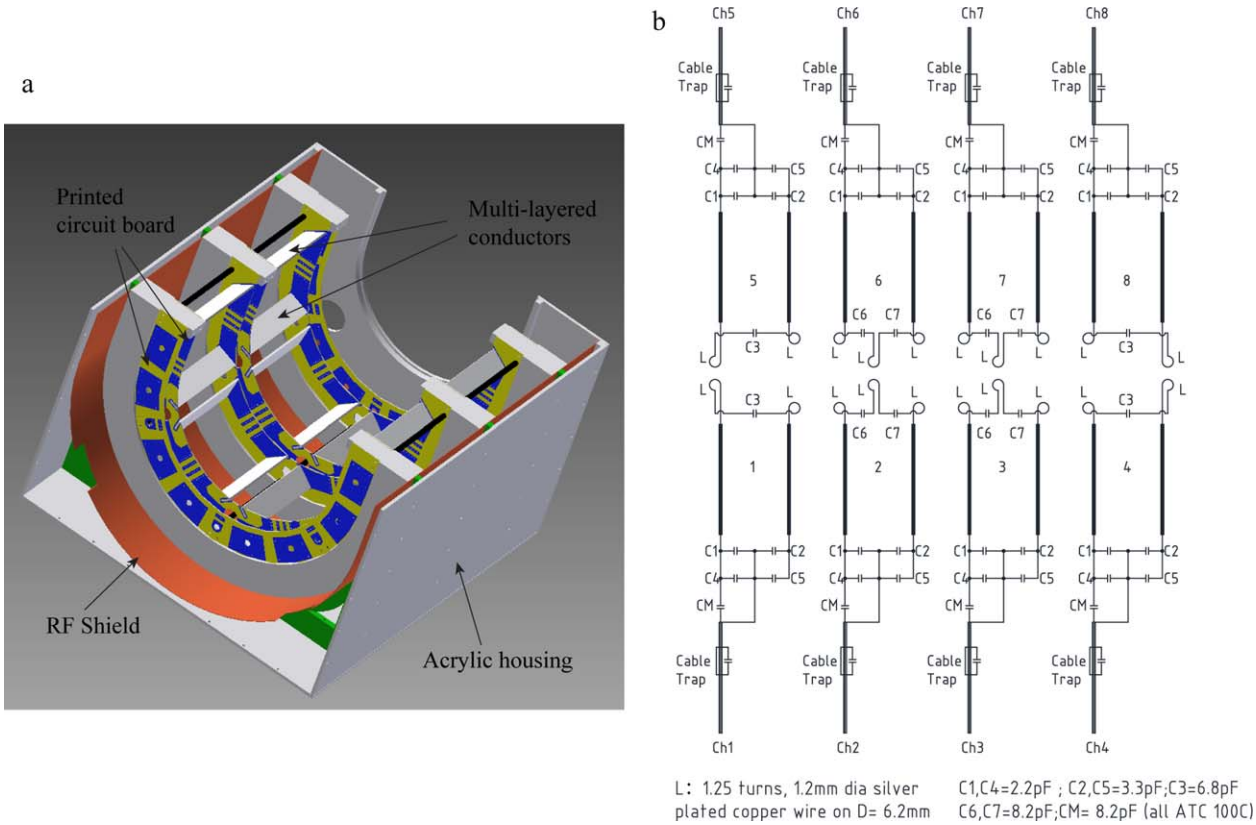

FIG. 1. (**a**) 3D model of the proposed pTx open RF coil model. (**b**) Simplified schematic of the multielement coil with values of the lumped elements used.

(Wilmington, Massachusetts, USA) (22,23) and the transceive quadrature ^{23}Na knee coil from Rapid MR International (Columbus, Ohio, USA) (24). Several important custom knee pTx coil developments have been implemented to improve transmission homogeneity, including a two-channel transmit coil in combination with the QED coil for reception at 7T (19) and a four-channel proton birdcage sodium transceiver array for multinuclei imaging (25). A multipurpose 16-channel pTx RF array has been developed by attaching microstrip transmission line elements to a malleable canvas, capable of conformable imaging of the knee (with eight active channels) (26). However, these custom 7T knee pTx coils cannot readily accommodate flexed joint postures for either static or dynamic imaging. To assist kinematic imaging, a "stretchable" receive array at 3T has been presented (27). However, this technique may not be suitable for transceive array applications at 7T due to higher resistive loss and variations of coil loading/coupling when stretched. A custom eight-channel pTx coil (28) has been developed for ankle imaging at 7T with an absence of dedicated commercial coils for this anatomical region. For ankle imaging, most studies have resorted to adapting an eight-channel pTx head coil (RAPID Biomedical, Rimpar, Germany) (14) or a quadrature head coil (19) with suboptimal signal-to-noise ratio performance, or used the cylindrical-shaped QED knee coil (13,20,29), which constrains imaging to the plantarflexed ankle joint.

In the present work, an eight-channel transceive array coil with pTx capability was designed and constructed for static and dynamic 7T MRI of the knee and ankle joints. The overall geometry used a U-shaped open design similar in profile to a previously reported ankle coil (28). In the current design, a suite of engineering aspects were optimized to provide high imaging performance at 7T for both the knee and ankle joints with comprehensive and conservative RF monitoring and safety procedures adopted during testing.

METHODS

Coil Design and Prototyping

Figure 1a shows a 3D model of the U-shaped open pTx coil. The eight rectangular loop elements were arranged in two cylindrical rows (diameter 180 mm and overall length 200 mm), providing extensive coverage in the head–foot direction. An RF shield was placed inside the coil housing 30 mm radially away from the array elements to reduce RF radiation and unwanted coupling from other system components. Figure 1b provides a simplified schematic of the eight-element coil, illustrating the rungs, capacitors for tuning (C1–C4), matching (CM) and inductors (L) for decoupling with neighboring elements. A photo of the constructed coil has been reported previously in a preliminary study (30), which also shows the stand-alone inductive loops used for decoupling with diagonal elements.

The two rungs of each element were made of multilayered stripline-like "sandwich" conductors for more uniform distribution of capacitance and inductance (31,32) compared with conventional designs using lumped elements. The dimensions of the dielectric and conductive materials were optimized to control the capacitance and inductance of the blades and hence, those of the coil elements. Discrete nonmagnetic high-voltage capacitors (American Technical Ceramics, Huntington Station, New York, USA; C-series) were soldered to the printed circuit boards connecting both ends of the sandwich blades for matching and additional tuning. The orientation of the sandwich blades was adjusted to improve B_1 penetration and alleviate mutual coupling between the coil elements (33). To further decouple neighboring elements, small counter-wound inductive decoupling loops (34) were formed in the corner or edge of each loop to introduce magnetic flux to counteract the coupling effects. The geometry of the sandwich blades, coil element, and array were optimized iteratively with numerical simulations conducted with Sim4Life by ZMT (https://www.zurich-medtech.com/sim4life/) using the finite-different time-domain solver. The optimized array showed decoupling better than −20 dB and port matching to 50 Ω better than −20 dB, when a knee joint model (full extension) was loaded. Because the matching and loading conditions vary across extended and flexed joint postures, the S-parameters for a variety of loading conditions are reported with bench measurements (see Results).

The coil housing was fabricated from laser-cut white acrylic sheet, assembled using acrylic cement and nonmagnetic screws. The shape of the housing, element positions, and cable placements were configured to permit imaging of either the left or right knee/ankle. S-parameters of the constructed coil were measured using a Vector Network Analyzer (ZNB8, Rohde & Schwarz GmbH & Co. KG, Munich, Germany). For subject safety, as well as protection of the MR system, each coil element was tested to withstand a peak RF power of 1 kW at 298.18 MHz. Specifically, a programmable synthesizer (HM8134-3; HAMEG Instruments GmbH, Munich, Germany) and an RF power amplifier (BLAH1000; Bruker BioSpin, Ettlingen, Germany) were used to produce a 20% duty-cycle rectangular pulse with a period of 4 ms and a peak power of 1 kW at 50 Ω. All eight channels were tested consecutively for 5 min under loaded conditions with no heating or arcing observed. The forward/reflected power levels as monitored using a four-channel oscilloscope (RTO1024, Rohde & Schwarz GmbH & Co. KG) showed no variation to baseline recordings when the power amplifier was connected to a high-power attenuator acting as a dummy load with monitoring capabilities.

MR System Integration

To interface the prototype coil to the 7T whole body research scanner (Siemens Healthcare, Erlangen, Germany), a dedicated transmit/receive (Tx/Rx) switch was developed in compliance with all specifications of the MRI system. The noise figure of the integrated low noise preamplifiers was less than 0.5. The maximum attenuation in the transmit path was 0.16 dB for each channel. An aluminum enclosure (Fig. 2) served to accommodate two PCBs of electronics. System specific plugs for the Tx and Rx paths were fitted to the aluminum enclosure, while eight individual RF connectors (85-QMA-S50-0-2; Huber+Suhner, Herisau, Switzerland) provided connections for the coil array. One additional multipin connector (LEMO, Ecublens, Switzerland) was used to provide the unique hardware coil code of the coil array to the MRI system. The Tx/Rx switch was verified to safely handle 1 kW peak RF power using the same procedure as for the coil array.

Electromagnetic Simulations and Virtual Observation Points

Numerical Electromagnetic Simulations

As illustrated in Supporting Figure S1, electromagnetic simulations with the final coil design were performed with two anatomically accurate posable voxel models [Duke and Ella from the virtual family (35)] in two different joint postures for both the knee and ankle. Specifically, the knee joint was simulated in 30° flexion and full extension, and the ankle joint in maximal dorsiflexion and plantarflexion. Lumped elements were used to fine tune each of the eight channels to resonate at 297.2 MHz and to match the input impedance to 50 Ω (reflection coefficient S_{11} better than −20 dB for all channels). Perfect decoupling was assumed by simulating each channel independently (on the same grid), while each simulation was allowed to converge to −40 dB. Electric field distributions were calculated with a harmonic voltage source with 1V amplitude and were exported to MATLAB (MathWorks, Natick, Massachusetts, USA) for processing/analysis.

RF Safety and Virtual Observation Points

To provide RF safety for the subjects, and protection for the RF hardware components, instantaneous, 10-s averaged, and 6-min averaged forward RF per-channel power levels were monitored automatically by the MR system and restricted to 100 W, 35 W, and 20 W, respectively. To provide further safety with respect to local SAR for the subjects, a comprehensive procedure was adopted to operate the coil well within the International Electrotechnical Commission guidelines (36). Instead of verifying the above limits for every 10 g of tissue, a smaller set ($n < 200$) of virtual observation points (VOPs) were monitored (37).

Specifically, for each electromagnetic simulation, a Q matrix (37) for each voxel (Q_{vox}) was generated from the simulated electric fields. The phases of the electric fields were adjusted to compensate for the relative phase delays introduced by different cable lengths between the coil plug and coil elements, as measured using a network analyzer. The 10-g Q matrices (Q_{10g}) were then calculated by averaging the Q_{vox} spatially over cubes containing exactly 10 g of tissue centered at the corresponding voxel (38). Finally, the Q_{10g} matrices of all the simulations for the respective joints were concatenated and compressed into a single set of VOPs using vendor-

d

S-Parameters Knee Extended

	#1	#2	#3	#4	#5	#6	#7	#8
#1	-21	-24	-20	-26	-19	-19	-26	-28
#2		-28	-20	-19	-21	-19	-33	-24
#3			-22	-33	-29	-39	-21	-26
#4				-27	-34	-27	-25	-20
#5					-20	-23	-20	-20
#6						-27	-18	-19
#7							-21	-24
#8								-21

S-Parameters Knee Flexed

	#1	#2	#3	#4	#5	#6	#7	#8
#1	-21	-31	-14	-17	-17	-27	-26	-30
#2		-12	-18	-14	-25	-24	-20	-20
#3			-12	-22	-25	-30	-20	-26
#4				-25	-37	-28	-23	-19
#5					-26	-25	-19	-20
#6						-24	-18	-19
#7							-16	-24
#8								-24

S-Parameters Ankle Neutral

	#1	#2	#3	#4	#5	#6	#7	#8
#1	-20	-27	-13	-14	-14	-28	-30	-26
#2		-14	-26	-13	-23	-24	-28	-27
#3			-15	-24	-24	-26	-23	-26
#4				-14	-26	-25	-28	-16
#5					-28	-15	-15	-18
#6						-17	-16	-16
#7							-27	-20
#8								-24

FIG. 2. (**a, b**) Illustration of the proposed 7T open pTx coil during imaging of the knee (a) and ankle joints (b). (**c**) Open pTx coil and interface enclosure with their connection in a top-down perspective. (**d**) Measured S-parameter matrices when the coil was loaded with a knee joint in full extension (left) and in 30° of flexion (middle) and an ankle joint in the neutral position (right).

supplied software. During the in vivo scans, the scanner's built-in function calculates the SAR values for each VOP and the considered time intervals (10 s and 6 min) and compares the worst-case results (SAR_{10g}) against the corresponding limits (20 and 10 W/kg, respectively). Both the knee and the ankle joint VOPs were derived by compressing the Q_{10g} matrices of four simulations, as detailed previously. A smaller overestimation rate results in more accurate SAR_{10g} calculation, but a larger number of VOPs (37). We found from experience that a large number of VOPs (exceeding 200) may prevent the scanner console (Syngo VB17 pTx, version 2.3) reliably updating the SAR_{10g} in real time for the sequences tested. For this reason, 15% and 6% overestimation rates were adopted for the knee and ankle joints during VOP compression, respectively. These were the lowest compression rates to generate no more than 200 VOPs (194 and 158 VOPs for the knee and ankle joints, respectively). Additionally, a global safety factor of 2 times was enforced on every VOP to account for variations in subjects' anatomy/positioning and inaccuracies in electromagnetic simulations.

MR Image Acquisition

Scanner and Volunteers

In healthy male volunteers, the knee (n = 2; age, 56, 52 years; weight, 91, 78 kg) and ankle joints (n = 2; age, 52, 25 years; weight, 78, 83 kg) were imaged using the pTx open coil on the 7T whole body research scanner, with a maximum gradient strength of 70 mT/m and a slew rate of 200 T/m/s). The volunteers had no history of clinically

Table 1
Sequence Protocol for Knee and Ankle Joints.

	TSE					
	PDw/ PDw-FatSat	T_1w	T_2w	DESS (Ankle)	MEDIC (Ankle)	BEAT-IRT (Larger FOV)
Acquisition time, min:s	3:40	4:09	3:47	5:28 (3:53)	5:29 (4:27)	0:50 (0:50)
Data matrix	512	512	512	448	448	160
Resolution, mm	0.3×0.3	0.3×0.3	0.3×0.3	0.47 iso	0.47 iso	1.0
Slice thickness, mm	2.5	2.5	2.5	NA	NA	3.0
FOV, mm	160	160	160	210	210	160 (200)
Number of slices	21	21	21	224 (176)	224 (176)	1
Flip angle	180°	180°	180°	18°	15°	45°
Bandwidth, Hz/pixel	271	271	271	399	399	1008
TE/TR, ms	26/5200	13/1100	105/9000	2.35/9.0	13/20	1.57/3.9 (1.44/3.5)
Turbo factor	11	2	2	NA	NA	NA
Grappa	2	2	3	2	3	2
Measurements	1	1	1	1	1	160 (270)

Abbreviations: BEAT-IRT, BEAT iterative real-time; DESS, dual-echo steady state; FOV, field of view; MEDIC, multiecho data image combination; NA, not available; PDw, proton density weighting; PDw-FatSat, proton density weighting with fat saturation; T_1w, T_1-weighted; T_2w, T_2-weighted; TE, echo time; TR, pulse repetition time; TSE, turbo spin echo.

significant knee or ankle pathology. The medical research ethics committee of the University of Queensland approved the current study, and informed written consent was obtained from all participants involved in the research.

Imaging Protocols

As shown in Figures 2a and 2b, the U-shaped open pTx coil allowed the knee and ankle joints to be imaged in prone and supine postures, respectively, enabling the assessment of the joints across multiple angles under both static and dynamic conditions. The knee joint was examined in postures from full extension to approximately 30° of flexion within the 60 cm bore of the magnet; imaging of the ankle joint was achieved across the full range of motion from maximal dorsiflexion to plantarflexion. The imaging sequences for both joints included a prototype gradient echo field map for B_0 shimming, a prototype turbo spin echo (TSE) with proton density-weighting (PDw), PDw with fat saturation, T_1 weighting (T_1w) and T_2 weighting (T_2w), 3D water-excited dual-echo steady state (we-DESS) sequence, and 3D multiecho data image combination (MEDIC) sequence. Dynamic images of the joints were acquired with a turbo-FLASH sequence (BEAT iterative real-time [BEAT-IRT]). The parameters of these sequences are listed in Table 1. The individual acquisition times of the static sequences were designed to be below 6 min to address patient comfort and minimize motion-related artefacts.

The static imaging protocols for the knee involved separate 25-min sessions with the joint first positioned in extension, then at approximately 30° flexion. As illustrated in Figure 2a, knee flexion was maintained by elevation of the lower leg by thick foam wedges. During the dynamic sequence, the subject was instructed to maintain a fully extended knee posture for the first 5 s of imaging, then to perform slow flexion-extension cycles (10 s) for the duration of the sequence (50 s). The initial 5 s of resting scans allowed the steady state of BEAT-IRT sequence to stabilize more quickly.

Static imaging of the ankle joint was performed at three angles (maximal plantarflexion, neutral, maximal dorsiflexion postures), with each separate session taking approximately 20 min. The neutral and dorsiflexion postures were maintained using foam wedges angled against the sole of the foot, while maximum plantarflexion was maintained by Velcro straps fastened across the dorsum of the foot. Similar to dynamic knee imaging, during dynamic imaging of the ankle joint the subjects maintained a neutral joint posture for the initial 5 s and then performed plantarflexion-dorsiflexion cycles (period = 10 se for the duration of sequence (50 s).

Coil Correlation Coefficient and Parallel Imaging Performance

The correlation coefficient matrix of the pTx coil was evaluated when loaded with a volunteer knee joint (full extension). The correlation coefficients were calculated from the channel individual raw data of a gradient echo sequence when the transmitter voltages were set to 0. The parallel imaging performance was evaluated with the same volunteer by measuring the receive sensitivity of the individual channels and calculating the geometric factor maps (g-maps) (39), for the central sagittal slice with anterior–posterior phase encoding and central coronal slice with left–right phase encoding. Reduction factors $R = 2$ and $R = 3$ were investigated, with a field of view (FOV) of 192 mm in the phase encoding directions.

B_1 Mapping and B_1 Shimming

Relative B_1 Mapping

A low flip angle gradient echo–based sequence (40) was employed to provide relative amplitude and phase B_1 maps for the 8 individual channels by consecutively transmitting on an individual channel, largely following a procedure described previously (41).

B_1 Shimming

B_1 shimming was performed in vivo using the vendor-supplied toolbox. The RF shimming volume for the knee

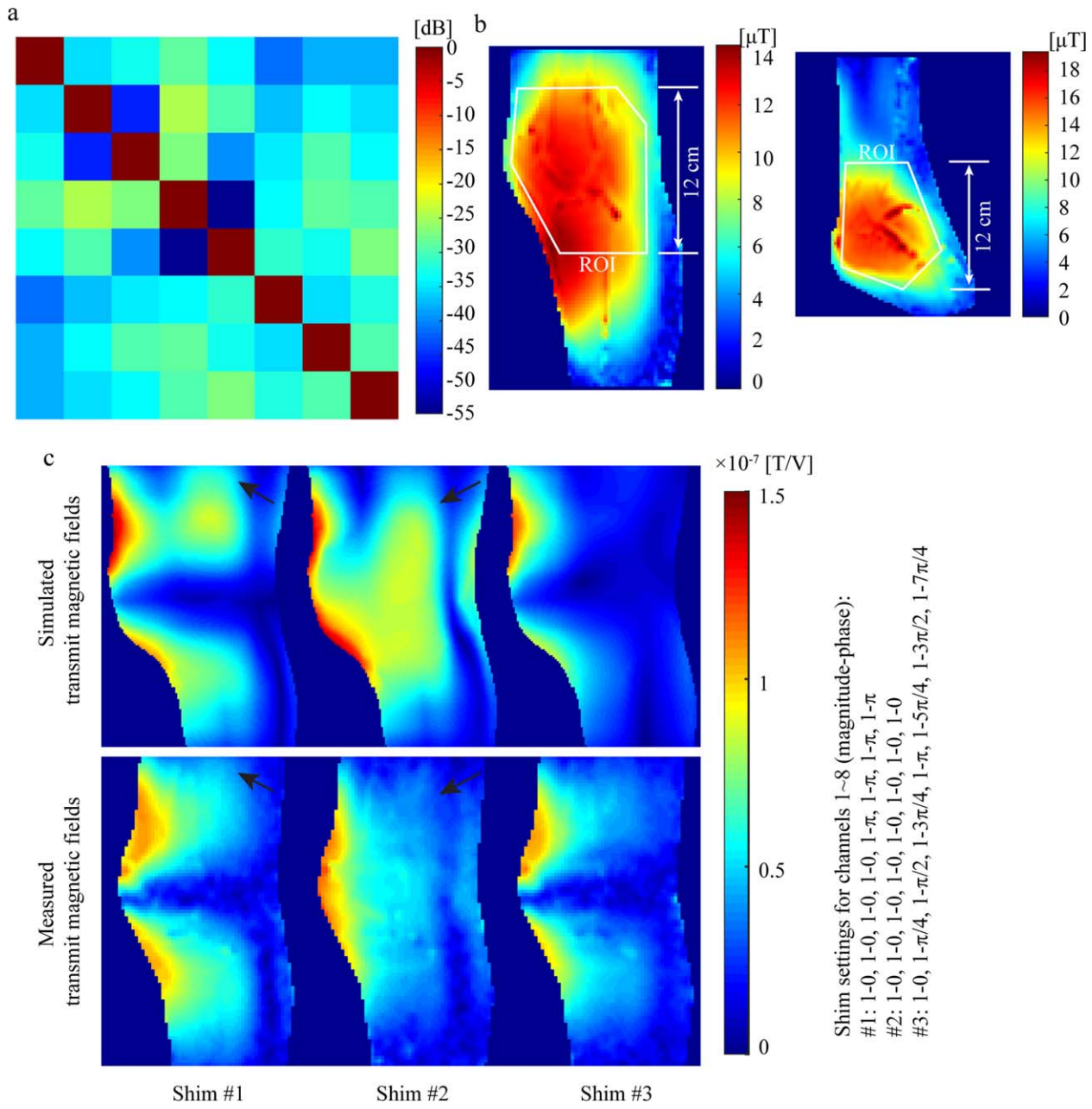

FIG. 3. (**a**) Coil channel correlation coefficient matrix in logarithmic scale. (**b**) Measured transmit magnetic fields with shim settings to produce maximum field magnitudes within the ROI for a knee joint (left) and an ankle joint (right). The maximum transmission magnitudes were 10.8 and 13.0 μT averaged over the ROIs for the knee and ankle joints, respectively, using the equipped 8 × 1 kW RF amplifiers. (**c**) Illustration of the simulated transmit magnetic fields (top) with three different shim settings compared with the measured counterparts (bottom).

region was chosen to include the patella, distal femur, and proximal tibia along with the joint menisci and cruciate ligaments and, in the ankle, the volume included the distal tibia, distal fibula, talus, and calcaneus along with the distal portion of the Achilles tendon.

Absolute B_1 Mapping

The absolute B_1 (or flip angle) was acquired using a vendor-supplied turbo FLASH (TFL)-based B_1 mapping sequence (42). To verify the numerical simulations, the transmit B_1 fields with a number of distinctive shim settings were acquired using this TFL-based B_1 mapping sequence and then compared with the calculated counterparts with the Duke model (43), as shown in Figure 3c. This comparison was performed for a fully extended knee joint and an ankle joint in plantarflexion with one of the volunteers for each joint, on similar sagittal slices and scaled to show the transmit B_1 fields per 1 V of transmission voltage per channel.

The TFL-based B_1 mapping sequence was also used to estimate the maximum achievable transmit B_1 field magnitude of the pTx coil with both joints on the central sagittal plane of the shim volume. To maximize the

transmit B_1 field, subject-individual phase-only shim settings were used, where the transmit voltages of the individual channels were kept identical, while their phases were calculated to provide constructive interferences. For each channel, the shim phase was determined as the negative of the average transmit phase within the ROI (indicated in Fig. 3b by polygons of approximately 120 mm length in the foot–head direction).

RESULTS

Coil Performance by Bench Measurements

The measured S-parameters of the pTx coil demonstrated good agreement with the simulated results, as shown in Figure 2d, including a knee joint in full extension and 30° of flexion and with an ankle joint in the neutral position. When the coil was loaded with a knee joint in the extended position (the optimal setup for the coil prototype), the measured S_{XX} values of all channels were better than −20 dB and S_{XY} −18 dB. As examples, the measured S-parameters of channels 1 and 2 with their nearest neighbors are shown in Supporting Figure S2. When the lower leg was flexed out of the coil, the matching conditions of the distal elements (i.e., #2 and #3) changed, resulting in a noticeable increase of reflection (though they remained better than −12 dB). The matching of the other elements did not change significantly, and the couplings among all channels were lower than −14 dB. When the coil was loaded with an ankle, elements #2, #3, #4, and #6 experienced loading changes, and hence increased reflection, whereas other elements were not noticeably affected. The highest coupling among channels with ankle imaging was −14 dB (i.e., S_{14} and S_{15}).

Noise Correlation and Parallel Imaging Performance

The correlation coefficient matrix of the pTx coil when loaded with a knee in full extension is shown in Figure 3a in dB scale. The noise correlation between any two different channels was found to be lower than 0.06 (−24 dB). When loaded with an anatomy different than a knee in full extension, the noise correlations among channels are expected to increase. The g-maps for the central sagittal slice and central coronal slice are shown in Supporting Figure S3. With the investigated scenarios, the maximum geometric factors were approximately 1.25 and 1.65 for $R = 2$ and $R = 3$, respectively. Parallel imaging with $R = 4$ in either the anterior–posterior or left–right direction is not advisable with the current pTx coil, because the maximum geometric factors were found to be approximately 3.5. However, as demonstrated by the imaging data that follow, reduction factor $R = 3$ can be employed without noticeable parallel imaging artifact.

B_1 Mapping and Maximum Transmit B_1 Magnitude

As shown in Figure 3c, the simulated transmit B_1 fields with the Duke model showed generally good agreement with the measured counterparts with three different shim settings. On average, the measured transmit B_1 magnitude is approximately 6% lower than the simulation over the shown FOV in the sagittal slice, which may be attributed to the losses in RF hardware components and/or the relaxation effect of the TFL-based B_1 mapping sequence. Additionally, there are noticeable local differences, such as in regions indicated in Figure 3c. The anatomical differences between the model and the in vivo subject played an important role here, as the voxel model was constructed in a supine position while the subject was in a prone position with leg tissues compressed against the patient table, creating obvious differences in overall shape, especially near the indicated regions. The local discrepancies are also likely to result from the difficulty of accurately simulating the interelement coupling of the coils, due to the use of inductive decoupling loops in the prototype coil. Previous work indicated that the neglect of decoupling generally makes the simulation models more likely to be conservative (44); however, more comprehensive studies are warranted in the future.

The maximum transmission transmit B_1 field magnitude of the coil with the knee and ankle joints are shown in Figure 3b with an FOV of 250 mm. With the equipped 8×1 kW amplifiers, the averaged transmit B_1 field magnitude within the ROIs were 10.8 and 13.0 μT for the knee and ankle joints with the displayed postures, respectively. With the applied phase-only shims, the inhomogeneity of the magnitude transmit B_1 fields (root mean square difference relative to the mean) within the respective ROIs was approximately 21% and 22% for the knee and ankle joints, respectively.

Static knee Imaging

The separate sessions for the static imaging of the knee joint (extended, flexed postures) took approximately 45 min, including time for B_0 shimming, B_1 mapping, and B_1 shimming. The dynamic sequence was performed in the first session after the static sequences. Figure 4 shows sagittal TSE images of the left knee joint in extended and flexed postures, both of which provide clear visualization of the ACL. A dedicated B_1 shim was successfully calculated and applied for each volunteer for each knee joint posture. In contrast, the circularly polarized (CP) mode produced substantial artifacts with complete signal nulls, as illustrated in the low-resolution PDw TSE images (Fig. 4a, 4f, 4k, and 4p). It was observed that the CP mode used at least twice as much peak RF power as the shim modes. Moreover, a concatenation of 2 was necessary to successfully perform the PDw TSE sequences in the CP mode. These series of images clearly demonstrated that dedicated RF shims are extremely useful not only for improved image homogeneity (especially for TSE sequences) but also for more efficient use of RF power. The latter in particular is essential for RF power intensive sequences (such as TSE), allowing additional slices/coverage within the same scan time. With subject specific shims, the ability of the open pTx coil to image joints at different postures with high quality can be clearly appreciated, offering additional examinations not possible with a conventional "closed" coil design. It is worth highlighting that the examinations were all performed well under the SAR

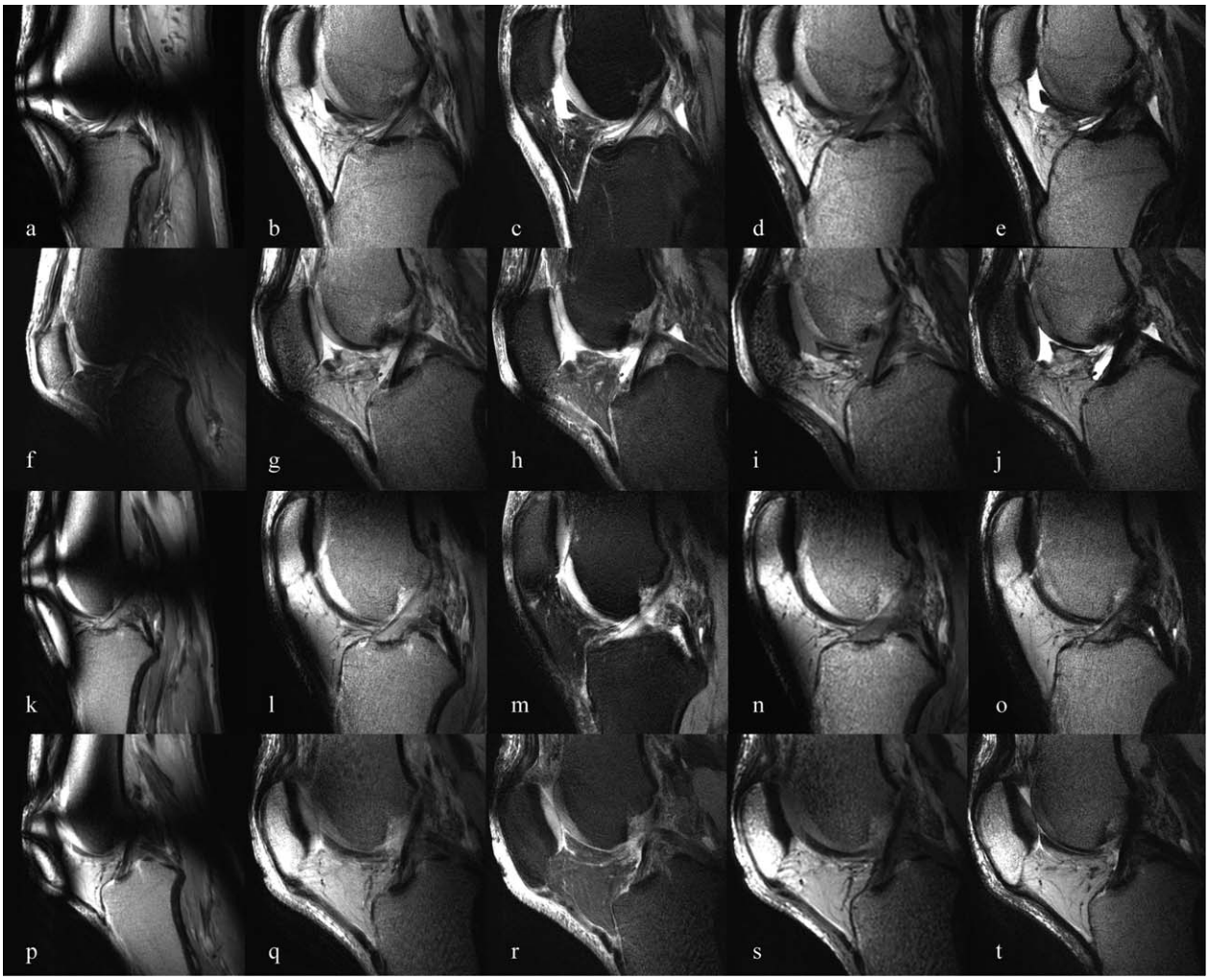

FIG. 4. Sagittal TSE images of the right knee of a 56-year-old man (**a–j**) and a 52-year-old man (**k–t**) acquired in both extended (a–e and k–o) and flexed (f–j and p–t) positions. To demonstrate the necessity of an adequate RF shimming, panels a, f, k, and p illustrate the artifacts associated with the CP mode, while the PDw (b, g, l, q), PDw with fat saturation (c, h, m, r), T_1w (d, i, n, s), and T_2w (e, j, o, t) images were acquired with individualized RF shimming at each position (see text for more details on RF shimming).

limits. The highest 10-s averaged SAR_{10g} was observed for the T_1w TSE sequence of the knee joint at 9.71 W/kg.

Figure 5 shows 3D we-DESS and 3D MEDIC knee joint images. Both DESS and MEDIC are useful for showing joint cartilage and fluid with the characteristic hypointense signal of cortical bone. In all cases, the delineation of various articular cartilage plates were evident. There was some incomplete water excitation, which may be improved with further optimization of the B_0 shimming routine and/or a central frequency adjustment that use all channels.

Dynamic Knee Imaging

Figure 6 shows a series of reconstructed temporal frames, in the sagittal plane, from dynamic imaging of the knee joint during flexion-extension cycles acquired with the BEAT-IRT sequence. As summarized in Table 1, while maintaining the same acquisition matrix, Figure 6 adopted an FOV of 160 mm and an in-plane resolution of 1×1 mm (3.25 frames per second) BEAT-IRT with a larger FOV of 200 mm and lower spatial resolution 1.25×1.25 mm was also acquired (Supporting Fig. S4), resulting in a higher temporal resolution of 5.2 frames per second. In both cases, the excursion of the ACL and posterior cruciate ligament were clearly visible, as was the vertical translation of the patella. The static B_1 shims determined with full extension of the knee joint were used without producing noticeable B_1 inhomogeneity during the dynamic scan. A signal drop at the lower leg was visible when it was flexed out of the coil (arrows in Fig. 6). However, this did not specifically affect the examination of the knee joint. Kinematic imaging of the knee joint is shown in Supporting Videos S1 and S2 at 1×1 mm and 1.25×1.25 mm in-plane resolution, respectively.

Static Ankle Protocol

The static imaging of the ankle involved two sessions, each taking approximately 45 min, with an initial session for the neutral position of the joint and a second session to acquire images for maximal dorsiflexion and maximal plantarflexion. The initial session for the neutral posture included all the static sequences (TSE images, we-DESS,

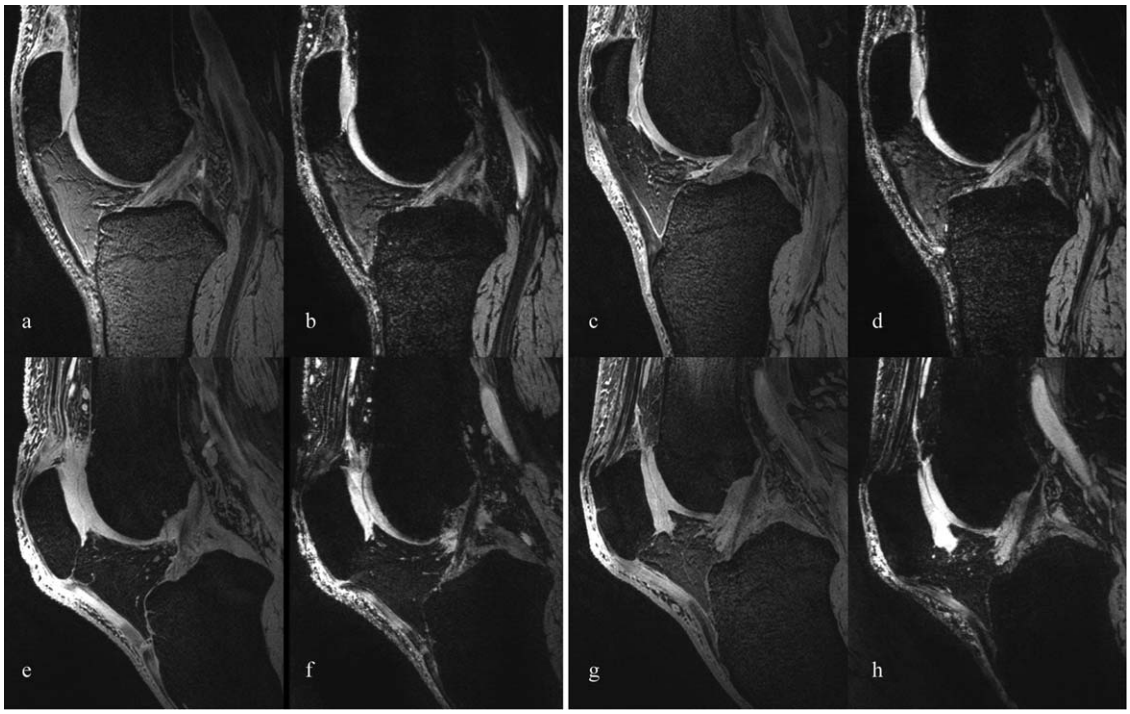

FIG. 5. Sagittal images from the 3D we-DESS (**a, c, e, g**) and MEDIC (**b, d, f, h**) series of the right knees in the 56-year-old (a, b, e, f) and 52-year-old (c, d, g h) volunteers. Images were taken in both extended (a–d) and flexed (e–h) joint positions.

and MEDIC) and all the preparation scans (B_0 shimming, B_1 mapping, and shimming). The second session included 3D static imaging (we-DESS and MEIDC) at both maximal dorsiflexion and maximal plantarflexion and the corresponding B_0 mapping sequences with both postures, as well as dynamic imaging. For the specific protocol of this study, it was found that the B_1 shim determined at the neutral position for the first volunteer successfully provided uniform excitation for the remaining ankle imaging sessions (including both volunteers and all sequences). This is understandable, considering that the ankle joint is considerably smaller than the knee joint, and the wavelength of the RF fields.

Figure 7 shows sagittal TSE images of the left ankle joints in the neutral position, which provide visualization of the Achilles tendon and the interosseous talocalcaneal ligament in the two volunteers. The CP mode produced major artifacts with complete signal nulls, as

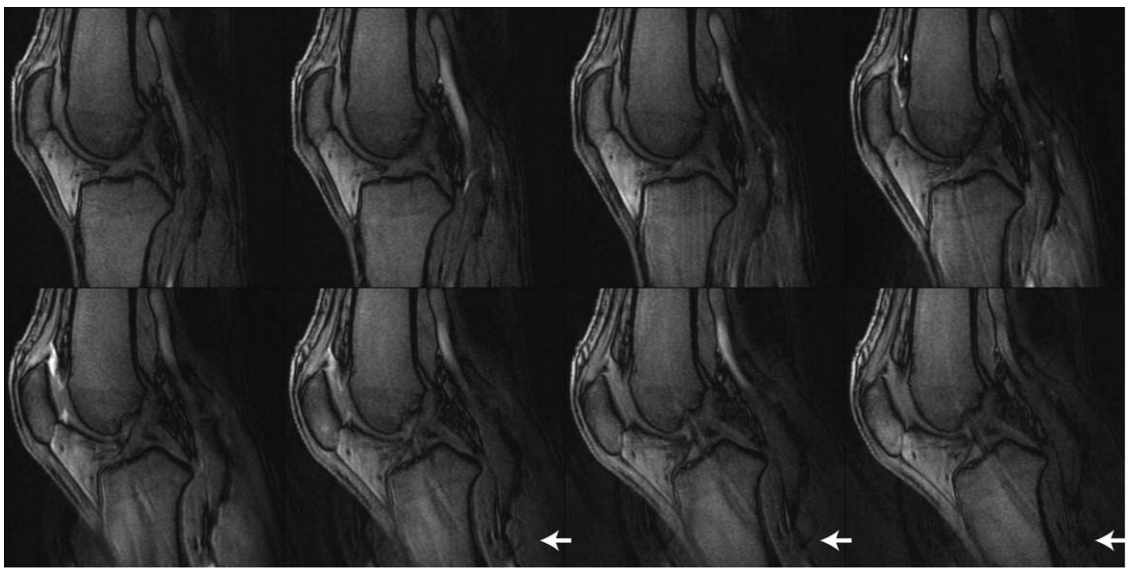

FIG. 6. Subset of frames from dynamic imaging of the right knee of the 56-year-old male volunteer at an in-plane resolution of 1×1 mm and a temporal resolution of 3.25 frames per second (see Table 1 for more details). A signal drop at the lower leg was visible when it was flexed out of the coil (arrows). A subset of frame with a higher temporal resolution is available with the Supporting Information, as are the dynamic videos (Supporting Videos S1 and S2).

FIG. 7. Sagittal TSE images of the right ankle joint of a 52-year-old man (**a–e**) and a 25-year-old man (**f–j**) acquired in the neutral position. Panels a and f illustrate the artifacts associated with the CP mode. PDw (b, g), PDw with fat saturation (c, h), T_1w (d, i), and T_2w (e, j) images were acquired with individualized shim modes.

illustrated in the low-resolution PDw TSE images (Fig. 7a,f), while the images have uniform intensity with the shim mode. Similar to the knee imaging sessions, the B_1 shims substantially reduced RF power and the local SAR maxima.

Figure 8 shows sagittal views of the ankle joints from the 3D we-DESS sequence obtained at maximal dorsiflexion and neutral and maximal plantarflexion postures in the two volunteers. The open design of the pTx coil allowed unobstructed joint postures, potentially

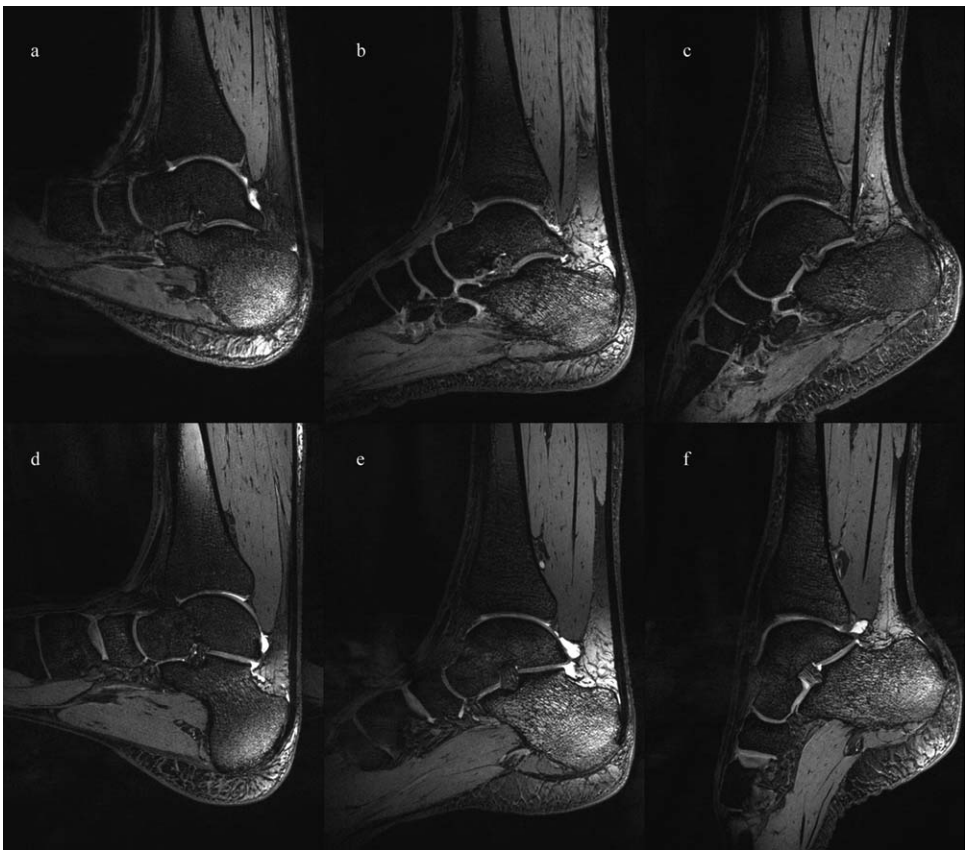

FIG. 8. Sagittal images from the 3D we-DESS of the right ankle joint of a 52-year-old man (**a–c**) and 25-year-old man (**d–f**) acquired at full dorsiflexion (a, d), neutral (b, e), and plantarflexion (c, f) positions.

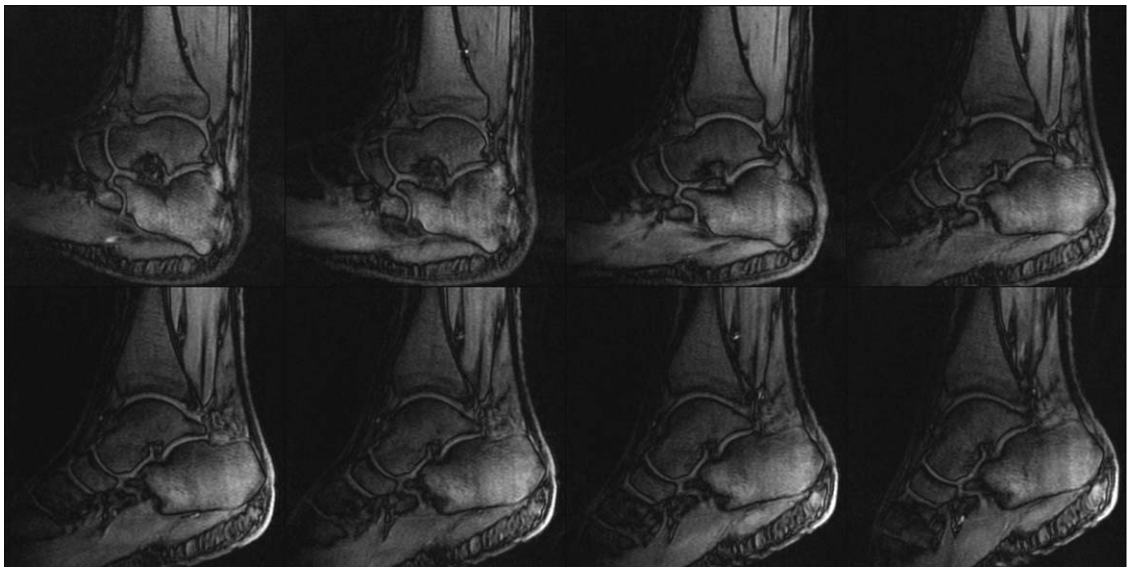

FIG. 9. Subset of frames obtained when dynamically flexing the right ankle of a 25-year-old male at an in-plane resolution of 1×1 mm and a temporal resolution of 3.25 frames per second (see Table 1 for more details). A subset of frames with a higher temporal resolution is available in the Supporting Information, as are the dynamic videos (Supporting Videos S3 and S4).

expanding diagnostic avenues compared with a conventional closed coil. The two volunteers had notably different ranges of joint motion, with volunteer 1 capable of more dorsiflexion (Fig. 8a versus Fig. 8d) and less plantarflexion (Fig. 8c versus 8f).

Dynamic Ankle Imaging

Figure 9 shows a series of reconstructed temporal frames of the sagittal view of the dynamic BEAT-IRT scans during ankle joint dorsiflexion and plantarflexion. Similar to the knee dynamic scans (Fig. 6), Figure 9 was acquired at a spatial resolution of 1×1 mm (see Table 1 for more details on sequence parameters), while a low-spatial and high-temporal resolution acquisition is shown in Supporting Figure S5. In both cases, changes in the width and length of the Achilles tendon were clearly visible during the motion of the ankle joint during the dynamic dorsiflexion-plantarflexion cycles. The B_1 shim produced uniform B_1 excitation over the FOV. Kinematic imaging of the ankle joint for the second volunteer is shown in Supporting Videos S3 and S4, at 1×1 mm and 1.25×1.25 mm in-plane resolution, respectively.

DISCUSSION

This work reports the design, implementation and successful application of a U-shaped pTx open coil dedicated for static and dynamic MRI of the human knee and ankle joints at 7 T. The overall coil design provides high transmit efficiency over a large 120 mm longitudinal ROI (maximum transmission fields of 10.8 and 13.0 μT for the knee and ankle joints, respectively) and good parallel imaging capability. It also allows easy access and positioning of the knee and ankle joints at multiple postures. As illustrated with in vivo imaging results, the design facilitates static imaging at various joint angles, and offers the capability to dynamically image actively moving joints. With adaption, the open design of the coil may provide extended applications in imaging of other joints (e.g., elbow) and extremity regions (e.g., calf, upper arm and forearm).

In the current study, specialized RF engineering techniques, such as stripline-line conductors, angularly-oriented blades and counter-wound inductive loops were employed. Combined with a low-loss interface and paired with the added benefit of RF shimming, this design enables a full coverage of the knee joint with 21 slices in sequences that are typically associated with a large SAR load and peak power requirement such as the T_1w TSE. Both the peak RF power and maximal local SAR were substantially below regulatory limits.

Future work to further improve image homogeneity will include investigation of advanced pTx techniques, such as multi-spoke RF pulses (45,46) or dynamically update the RF shims dependent on the joint's position. With the experience gained from the current study, further optimization in the design of the coil is envisaged where, without sacrificing the range of joint motion, the addition of RF elements would provide more sensitivity at the top of the array (anteriorly for supine ankle imaging and posteriorly for prone knee imaging). This can be achieved by reducing the FOV in the head-foot direction and/or introducing a number of dependent RF elements whilst taking full advantage of the available eight independent RF transmit channels.

In conclusion, we present a versatile new pTx coil for dedicated MRI of the knee and ankle joints at 7T. It conformably accommodates the knee and ankle for static imaging across different joint angles, as well as dynamic imaging during continuous flexion-extension cycles. Various engineering techniques have been included to provide an efficient implementation to balance the available RF power, desired flip angle (e.g., large flip angle

refocusing pulses in TSE sequences) and SAR limits for in vivo applications on a 7T whole-body MR system.

ACKNOWLEDGMENTS

Jin Jin, Ewald Weber, and Aurelien Destruel contributed equally to this work. We thank ZMT Zurich MedTech AG for providing the electromagnetic simulation software package SIM4LIFE. We also thank Markus Barth and Desmond Tse at the Centre for Advanced Imaging, University of Queensland, for valuable discussions.

REFERENCES

1. Link TM, Sell CA, Masi JN, Phan C, Newitt D, Lu Y, Steinbach L, Majumdar S. 3.0 vs 1.5 T MRI in the detection of focal cartilage pathology—ROC analysis in an experimental model. Osteoarthritis and Cartilage 2006;14:63–70.
2. Kraff O, Fischer A, Nagel AM, Mönninghoff C, Ladd ME. MRI at 7 Tesla and above: demonstrated and potential capabilities. J Magn Reson Imaging 2015;41:13–33.
3. Vaughan JT, Garwood M, Collins CM, et al. 7T vs. 4T: RF power, homogeneity, and signal-to-noise comparison in head images. Magn Reson Med 2001;46:24–30.
4. Schick F. Whole-body MRI at high field: technical limits and clinical potential. Eur Radiol 2005;15:946–959.
5. Robitaille PML, Abduljalil AM, Kangarlu A, et al. Human magnetic resonance imaging at 8 T. NMR Biomed 1998;11:263–265.
6. Regatte RR, Schweitzer ME. Ultra-high-field MRI of the musculoskeletal system at 7.0T. J Magn Reson Imaging 2007;25:262–269.
7. Homann H, Graesslin I, Eggers H, Nehrke K, Vernickel P, Katscher U, Dössel O, Börnert P. Local SAR management by RF shimming: a simulation study with multiple human body models. MAGMA 2012;25:193–204.
8. Katscher U, Bornert P, Leussler C, van den Brink JS. Transmit SENSE. Magn Reson Med 2003;49:144–150.
9. Zhu Y. Parallel excitation with an array of transmit coils. Magn Reson Med 2004;51:775–784.
10. Ibrahim TS, Lee R, Baertlein BA, Abduljalil AM, Zhu H, Robitaille P-ML. Effect of RF coil excitation on field inhomogeneity at ultra high fields: a field optimized TEM resonator. Magn Reson Imaging 2001;19:1339–1347.
11. Van den Berg CAT, Van den Bergen B, de Kamer JBV, Raaymakers BW, Kroeze H, Bartels LW, Lagendijk JJW. Simultaneous B1 + homogenization and specific absorption rate hotspot suppression using a magnetic resonance phased array transmit coil. Magn Reson Med 2007;57:577–586.
12. Hsu Y-C, Chern IL, Zhao W, Gagoski B, Witzel T, Lin F-H. Mitigate B1 + inhomogeneity using spatially selective radiofrequency excitation with generalized spatial encoding magnetic fields. Magn Reson Med 2014;71:1458–1469.
13. Juras V, Welsch G, Bär P, Kronnerwetter C, Fujita H, Trattnig S. Comparison of 3 T and 7 T MRI clinical sequences for ankle imaging. Eur J Radiol 2012;81:1846–1850.
14. Theysohn JM, Kraff O, Maderwald S, Kokulinsky PC, Ladd ME, Barkhausen J, Ladd SC. MRI of the ankle joint in healthy nonathletes and in marathon runners: image quality issues at 7.0 T compared to 1.5 T. Skeletal Radiol 2013;42:261–267.
15. Dean Deyle G. The role of MRI in musculoskeletal practice: a clinical perspective. J Man Manip Ther 2011;19:152–161.
16. Marques J, Genant HK, Lillholm M, Dam EB. Diagnosis of osteoarthritis and prognosis of tibial cartilage loss by quantification of tibia trabecular bone from MRI. Magn Reson Med 2013;70:568–575.
17. Kaiser J, Bradford R, Johnson K, Wieben O, Thelen DG. Measurement of tibiofemoral kinematics using highly accelerated 3D radial sampling. Magn Reson Med 2013;69:1310–1316.
18. d'Entremont AG, Nordmeyer-Massner JA, Bos C, Wilson DR, Pruessmann KP. Do dynamic-based MR knee kinematics methods produce the same results as static methods? Magn Reson Med 2013;69:1634–1644.
19. Larson PEZ, Han M, Krug R, Jakary A, Nelson SJ, Vigneron DB, Henry RG, McKinnon G, Kelley DAC. Ultrashort echo time and zero echo time MRI at 7T. MAGMA 2016;29:359–370.
20. Deligianni X, Bär P, Scheffler K, Trattnig S, Bieri O. High-resolution Fourier-encoded sub-millisecond echo time musculoskeletal imaging at 3 T and 7 T. Magn Reson Med 2013;70:1434–1439.
21. Kraff O, Theysohn JM, Maderwald S, Saylor C, Ladd SC, Ladd ME, Barkhausen J. MRI of the knee at 7.0 Tesla. Fortschr Röntgenstr 2007;179:1231–1235.
22. Stahl R, Krug R, Kelley DAC, Zuo J, Ma CB, Majumdar S, Link TM. Assessment of cartilage-dedicated sequences at ultra-high-field MRI: comparison of imaging performance and diagnostic confidence between 3.0 and 7.0 T with respect to osteoarthritis-induced changes at the knee joint. Skeletal Radiol 2009;38:771–783.
23. Banerjee S, Krug R, Carballido-Gamio J, Kelley DAC, Xu D, Vigneron DB, Majumdar S. Rapid in vivo musculoskeletal MR with parallel imaging at 7T. Magn Reson Med 2008;59:655–660.
24. Wang L, Wu Y, Chang G, Oesingmann N, Schweitzer ME, Jerschow A, Regatte RR. Rapid Isotropic 3D-Sodium MRI of the knee joint in-vivo at 7T. J Magn Reson Imaging 2009;30:606–614.
25. Brown R, Madelin G, Lattanzi R, Chang G, Regatte RR, Sodickson DK, Wiggins GC. Design of a nested eight-channel sodium and four-channel proton coil for 7T knee imaging. Magn Reson Med 2013;70:259–268.
26. Wu B, Zhang X, Wang C, Li Y, Pang Y, Lu J, Xu D, Majumdar S, Nelson SJ, Vigneron DB. Flexible Transceiver array for ultrahigh field human MR imaging. Magn Reson Medicine 2012;68:1332–1338.
27. Nordmeyer-Massner JA, De Zanche N, Pruessmann KP. Stretchable coil arrays: Application to knee imaging under varying flexion angles. Magn Reson Med 2012;67:872–879.
28. Orzada S, Bitz AK, Schäfer LC, Ladd SC, Ladd ME, Maderwald S. Open design eight-channel transmit/receive coil for high-resolution and real-time ankle imaging at 7 T. Med Phys 2011;38:1162–1167.
29. Juras V, Zbyn S, Pressl C, Valkovic L, Szomolanyi P, Frollo I, Trattnig S. Regional variations of T_2^* in healthy and pathologic achilles tendon in vivo at 7 T: preliminary results. Magn Reson Med 2012;68:1607–1613.
30. Henin B, Weber E, Crozier S. A novel 8-channel transceive open knee coil for dynamic musculoskeletal imaging at 7 Tesla. In Proceedings of the 24th Annual Meeting of ISMRM, Singapore, 2016. p 3517.
31. Weber E, Li BK, Liu F, Crozier S. A ultra high field multi-element transceive volume array for small animal MRI. Conf Proc IEEE Eng Med Biol Soc 2008;2008:2039–2042.
32. Li Y, Weber E, Liu F, Li BK, Crozier S. The optimization of an 8-channel transceive volume array for small animal MRI at 9.4T. Conf Proc IEEE Eng Med Biol Soc 2011;2011:2833–2836.
33. Li BK, Liu F, Weber E, Crozier S. Hybrid numerical techniques for the modelling of radiofrequency coils in MRI. NMR Biomed 2009;22:937–951.
34. Crozier S, Li BK, Liu F, Weber E, inventors; University of Queensland, assignee. MRI coil design. Google patent EP2281208 A4; June 13, 2012.
35. Andreas C, Wolfgang K, Eckhart GH, et al. The Virtual Family—development of surface-based anatomical models of two adults and two children for dosimetric simulations. Phys Med Biol 2010;55:N23.
36. International Electrotechnical Commission. International standard, medical equipment—part 2-33: particular requirements for the safety of magnetic resonance equipment. Volume 60601. Geneva, Switzerland: International Electrotechnical Commission; 2002.
37. Eichfelder G, Gebhardt M. Local specific absorption rate control for parallel transmission by virtual observation points. Magn Reson Med 2011;66:1468–1476.
38. Caputa K, Okoniewski M, Stuchly MA. An algorithm for computations of the power deposition in human tissue. IEEE Antennas and Propagation Magazine 1999;41:102–107.
39. Pruessmann KP, Weiger M, Scheidegger MB, Boesiger P. SENSE: sensitivity encoding for fast MRI. Magn Reson Med 1999;42:952–962.
40. Chung S, Kim D, Breton E, Axel L. Rapid B1 + mapping using a preconditioning RF pulse with TurboFLASH readout. Magn Reson Med 2010;64:439–446.
41. Van de Moortele PF, Ugurbil K. Very fast multi channel B1 calibration at high field in the small flip angle regime. In Proceedings of the 10th Annual Meeting of ISMRM, Honolulu, Hawaii, USA, 2009. p 367.
42. Haase A. Snapshot flash MRI. Applications to T1, T2, and chemical-shift imaging. Magn Reson Med 1990;13:77–89.
43. Hoffmann J, Henning A, Giapitzakis IA, Scheffler K, Shajan G, Pohmann R, Avdievich NI. Safety testing and operational procedures

for self-developed radiofrequency coils. NMR Biomed 2016;29:1131–1144.
44. Beqiri A, Hand JW, Hajnal JV, Malik SJ. Comparison between simulated decoupling regimes for specific absorption rate prediction in parallel transmit MRI. Magn Reson Med 2015;74:1423–1434.
45. Cloos MA, Boulant N, Luong M, Ferrand G, Giacomini E, Le Bihan D, Amadon A. kT-points: short three-dimensional tailored RF pulses for flip-angle homogenization over an extended volume. Magn Reson Med 2012;67:72–80.
46. Schmitter S, DelaBarre L, Wu X, Greiser A, Wang D, Auerbach EJ, Vaughan JT, Uğurbil K, Van de Moortele P-F. Cardiac imaging at 7 T: single- and two-spoke radiofrequency pulse design with 16-channel parallel excitation. Magn Reson Med 2013;70:1210–1219.

SUPPORTING INFORMATION

Additional Supporting Information may be found in the online version of this article.

Fig. S1. Illustration of the configurations of the proposed pTx open RF coil model and posable voxel human model (Duke) used for knee imaging (**a, b**) and ankle imaging (**c, d**). The Ella voxel model was configured similarly.
Fig. S2. The measured S-parameters of coil elements 1 (left) and 2 (right) with neighboring coil elements.
Fig. S3. The in vivo geometric factor (g-factor) maps for acceleration in anterior–posterior (top) and left–right directions (bottom) for acceleration factor $R = 2$ (left) and $R = 3$ (right).
Fig. S4. A subset of frames from dynamic imaging of the right knee of a 56-year-old man at an in-plane resolution of 1.25×1.25 mm and a temporal resolution of 5.2 frames per second (see Table 1 for more details).
Fig. S5. Subset of frames obtained when dynamically flexing the right ankle of a 25-year-old man at an in-plane resolution of 1.25×1.25 mm and a temporal resolution of 5.2 frames per second (see Table 1 for more details).
Video S1. Dynamic video of continuous knee flexion-extension motion cycles in a 52-year-old man acquired with the BEAT-IRT sequence at a sagittal slice across the ACL. Data were acquired at $1 \times 1 \times 3$ mm spatial resolution and at 3.25 frames per second (see Table 1 for more details).
Video S2. Dynamic video of continuous knee flexion-extension motion cycles in a 52-year-old man acquired with the BEAT-IRT sequence at a sagittal slice across the ACL. Data were acquired at $1.25 \times 1.25 \times 3$ mm spatial resolution and at 5.2 frames per second.
Video S3. Dynamic video of continuous ankle flexion-extension motion cycles in a 25-year-old man acquired with the BEAT-IRT sequence at a sagittal slice across the Achilles tendon. Data were acquired at $1 \times 1 \times 3$ mm spatial resolution and at 3.25 frames per second (see Table 1 for more details).
Video S4. Dynamic video of continuous ankle flexion-extension motion cycles in a 25-year-old man acquired with the BEAT-IRT sequence at a sagittal slice across the Achilles tendon. Data were acquired at $1.25 \times 1.25 \times 3$ mm spatial resolution and at 5.2 frames per second.